Check for updates

Localized thermal spike driven morphology and electronic structure transformation in swift heavy ion irradiated TiO₂ nanorods†

Sutapa Dey, [ID] [a] Anusmita Chakravorty,[b] Shashi Bhusan Mishra, [ID] [c] Nasima Khatun, [ID] [a] Arnab Hazra,[d] Birabar Ranjit Kumar Nanda, [ID] [c] Chandran Sudakar, [ID] [e] Debdulal Kabiraj[b] and Somnath C. Roy [ID] ⋆[a]

Irradiation of materials by high energy (∼MeV) ions causes intense electronic excitations through inelastic transfer of energy that significantly modifies physicochemical properties. We report the effect of 100 MeV Ag ion irradiation and resultant localized (∼few nm) thermal spike on vertically oriented TiO₂ nanorods (∼100 nm width) towards tailoring their structural and electronic properties. Rapid quenching of the thermal spike induced molten state within ∼0.5 picosecond results in a distortion in the crystalline structure that increases with increasing fluences (ions per cm²). Microstructural investigations reveal ion track formation along with a corrugated surface of the nanorods. The thermal spike simulation validates the experimental observation of the ion track dimension (∼10 nm diameter) and melting of the nanorods. The optical absorption study shows direct bandgap values of 3.11 eV (pristine) and 3.23 eV (5 × 10¹² ions per cm²) and an indirect bandgap value of 3.10 eV for the highest fluence (5 × 10¹³ ions per cm²). First principles electronic structure calculations corroborate the direct-to-indirect transition that is attributed to the structural distortion at the highest fluence. This work presents a unique technique to selectively tune the properties of nanorods for versatile applications.

1. Introduction

Manipulation of physical and chemical properties of materials through modification of crystallinity, morphology and electronic structure is of great interest to researchers.[1,2] High energy ion beam irradiation is a unique technique, which induces localized modification in a material without the irradiating ions being implanted or doped into the lattice.[3–6] When an energetic ion travels through a material, it transfers its energy to the atomic and electronic subsystems in two ways, which are called nuclear/elastic energy loss (S_n) and electronic/inelastic energy loss (S_e). In general, if the energy of an ion exceeds 1 MeV per

[a]Semiconducting Oxide Materials, Nanostructures and Tailored Heterojunction (SOMNaTH) Lab, Functional Oxide Research Group (FORG), Department of Physics, Indian Institute of Technology Madras, Chennai 600036, India. E-mail: somnath@iitm.ac.in

[b]Inter-University Accelerator Centre, Aruna Asaf Ali Marg, New Delhi 110067, India

[c]Condensed Matter Theory and Computational Lab, Department of Physics and Center for Atomistic Modelling and Materials Design (CAMMD), Indian Institute of Technology Madras, Chennai 600036, India

[d]Department of Electrical & Electronics Engineering, Birla Institute of Technology & Science-Pilani, Pilani Campus, Pilani-333031, Rajasthan, India

[e]Multifunctional Materials Laboratory, Department of Physics, Indian Institute of Technology Madras, Chennai 600036, India

† Electronic supplementary information (ESI) available. See DOI: 10.1039/d1na00666e

nucleon, it is called the swift heavy ion (SHI), where S_e dominates over S_n. When S_e becomes larger than a threshold value, the huge energy deposited by an ion creates a latent track along its trajectory with a cross-section of a few nanometers.[7] The track is a region of distinguishable crystallinity depending on the type of target material, ion energy, and the type of ion chosen. Thus, SHI irradiation provides flexibility to selectively modify the target material in a highly localized manner.

Titanium dioxide (TiO₂) remains one of the most prominent members of the metal oxide family owing to its high chemical and thermal stability, excellent photoactivity, biocompatibility and availability in the form of three different polymorphs (anatase, brookite and rutile).[8,9] There are a few reports, which have discussed SHI irradiation-induced structural changes in TiO₂, for example, from amorphous to anatase,[10] rutile,[11,12] and mixed-phase;[12] and anatase to amorphous,[13] rutile,[14] and mixed-phase[15] transformations. SHI irradiation induced effects have also been studied on doped TiO₂. For example, Gautam et al.[16] reported 120 MeV Ag and 130 MeV Ni ion induced phase transformation in undoped and niobium doped anatase TiO₂ composite thin films. Thakurdesai et al. observed a SHI-induced phase transition of a pulsed laser deposited TiO₂ thin film from the rutile to the anatase phase.[17] SHI-induced nano or microlithography[18–21] has been reported on single crystal rutile TiO₂. Further, formation of the ion track under SHI irradiation has been investigated in single crystal rutile TiO₂ with (001),[22,23]

(110),[24–26] and (100)[27] orientations. Latent tracks of different morphologies such as cylindrical, dumbbell-shaped or sandglass-like have been observed with variation of ion path length as a consequence of molten phase outflow and recrystallization.[28] In the case of thin films, 120 MeV Ag ion irradiation has been performed on a rutile TiO_2 film deposited by ion beam sputtering on silicon to investigate the influence of SHI irradiation on the dynamics of phonon interactions.[29] Rath *et al.* reported 79 MeV Br ion induced modifications in a 200 nm thick rutile TiO_2 thin film prepared by DC magnetron sputtering on a Si (100) substrate.[30] The sample crystallinity was retained up to a fluence of 1×10^{13} ions per cm^2, even though the S_e value exceeded the threshold for amorphization along the ion track in TiO_2.[30] Some of the important published studies on Ag ion irradiation effects on TiO_2 are listed in Table T1 (ESI†). It is therefore apparent that several studies have been reported on SHI irradiation of TiO_2 single-crystal and thin films; however, such studies on TiO_2 nanostructures remain unexplored.

One-dimensional nanostructures such as nanowires and nanorods, offer the advantage of unidirectional charge transport along with high specific surface area.[31] Particularly, highly aligned and vertically oriented TiO_2 nanorods hydrothermally grown on a fluorine doped tin oxide (FTO) coated glass substrate have shown strong potential in applications such as electrode materials with a transparent conducting window for solar cells,[32] water splitting,[33] electrocatalysis,[34] bio-photoelectrochemical reactions,[35] UV photodetectors,[36] electron transport layers in perovskite solar cells,[37] electron injection layers in DSSCs,[38] sensors,[39] *etc.* In addition, the single-crystalline nature of each nanorod provides a long-range periodicity throughout the individual nanorod structure, which is a suitable platform for the study of irradiation effects. Moreover, a small lateral dimension (a few tens of nanometers) of the nanorods provides limited space for thermal energy transfer and atomic displacement in the radial direction. Therefore, it is interesting to explore the effect of SHI irradiation-induced localized energy transfer in rutile TiO_2 nanorods. Here, we present the crystalline phase, morphology and electronic structure transformation of the SHI (100 MeV Ag ion) irradiated TiO_2 nanorods, and their effect on the optical absorption. The experimental data and observation are correlated with the thermal spike model-based analysis and density functional theory (DFT) calculated band structure to gain an insight into ion beam-induced disorder and defects in these nanorods.

2.   Experimental section

2.1.   Preparation of TiO₂ nanorod arrays

TiO_2 nanorod arrays were synthesized by a hydrothermal method on a FTO coated glass substrate. The details of the synthesis process are given in our previous report.[40] Briefly, the hydrothermal process was carried out at 200 °C for 2 hours, where the reaction solution comprised 10 ml of concentrated hydrochloric acid (HCl 37%), 10 ml of de-ionized (DI) water, and 0.3 ml of titanium(IV) butoxide. The as-prepared TiO_2 nanorod samples were rinsed thoroughly with DI water, air-dried, and

finally annealed at 450 °C for 30 minutes to ensure the stability of TiO_2 nanorods on the substrate.

2.2.   Experimental details of ion irradiation

The TiO_2 nanorods grown on a FTO coated glass substrate were irradiated at room temperature with 100 MeV Ag ions using the 15UD accelerator at the Inter-University Accelerator Centre, New Delhi, India.[41] The fluences used for irradiation were 1×10^{12}, 5×10^{12}, 1×10^{13} and 5×10^{13} ions per cm^2. The beam current was maintained at $\sim$7 nA to avoid any joule heating. The Stopping and Range of Ions in Matter (SRIM)[42] code was used to calculate the electronic energy loss and range of the ion inside the material.

2.3.   Characterization

A field emission scanning electron microscope (FESEM) (Model-FEI Inspect F50), operating at 30 keV, was employed to study the surface morphology. X-ray diffraction (XRD) patterns were recorded using a RigakuSmartLab X-ray Diffractometer with Cu K_α ($\lambda = 0.154$ nm), operating at 45 kV and 200 mA anode current. Raman spectroscopy was performed using the HORIBA LabRAM HR instrument equipped with an argon ion laser emitting 488 nm (2.54 eV) excitation wavelength. A transmission electron microscope (TEM) (Model-Tecnai G2 T20), operating at an accelerating voltage of 200 kV, was used to observe the microstructure and record the electron diffraction pattern. An X-ray photoelectron spectrometer (ESCAprobe TPD), equipped with an Mg K_α X-ray source, was employed to perform X-ray photoelectron spectroscopy (XPS). Optical absorption spectroscopy was carried out using a PerkinElmer LAMBDA 950 UV-Vis-NIR Spectrophotometer, equipped with an integrating sphere accessory, and operating in diffuse reflectance mode. Photoluminescence (PL) spectra were acquired using a JobinY-vonFluorimeter (Fluorolog-3-11), equipped with a Xe lamp source and a photomultiplier tube detector.

3.   Results and discussion

3.1.   Morphology, crystallinity, microstructure and chemical composition analysis

The surface morphologies of the pristine and irradiated TiO_2 nanorod arrays investigated through FESEM images are presented in Fig. 1. The pristine TiO_2 nanorods are shown in Fig. 1(a). It is observed that the individual rods are tetragonal in shape with a length of $\sim$1 μm and an average width of $\sim$100 nm. The surface morphologies of the samples after irradiation at different fluences (1×10^{12}, 5×10^{12}, 1×10^{13} and 5×10^{13} ions per cm^2) are shown in Fig. 1(b), (c), (d) and (e) respectively. The range of 100 MeV Ag in TiO_2 (density 4.25 g cm^{-3}), estimated using the SRIM code,[42] is 8.85 μm, which ensures that all irradiating ions pass through the nanorod structure ($\sim$1 μm long) without being implanted or doped in the material.

At a low fluence of 1×10^{12} ions per cm^2, no significant changes are observed (Fig. 1(b)). However, the nanorod structures show slight bending at a few locations (Fig. 1(c)) after irradiation at a fluence of 5×10^{12} ions per cm^2 (indicated by
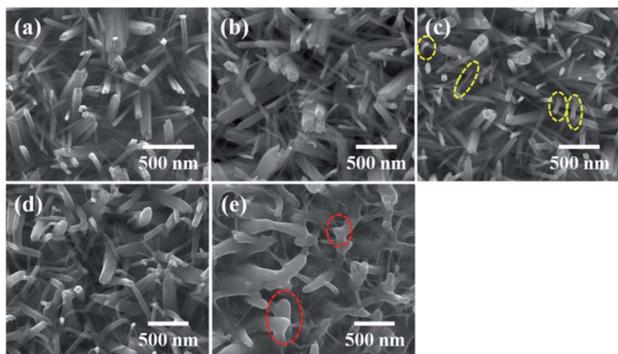
Fig. 1 FESEM images of (a) pristine and irradiated samples with (b) 1×10^{12}, (c) 5×10^{12}, (d) 1×10^{13} and (e) 5×10^{13} ions per cm^2 fluences. Yellow ellipses in (c) indicate slight bending of nanorods, and red ellipses in (e) indicate interconnected adjacent nanorods.

Fig. 2 (a) XRD patterns of pristine and irradiated samples at fluences of 1×10^{12}, 5×10^{12}, 1×10^{13} and 5×10^{13} ions per cm^2; high-resolution XRD peaks corresponding to (b) (101) and (c) (211) crystallographic planes of rutile TiO$_2$ respectively for pristine and irradiated (at a fluence of 1×10^{12} ions per cm^2 samples.

yellow ellipses), followed by an increase in bending and morphological distortion at a fluence of 1×10^{13} ions per cm^2 (Fig. 1(d)). Further increase of fluence to 5×10^{13} ions per cm^2 causes a significant structural distortion and bending of individual nanorods with the appearance of a semi-transparent layer connecting the adjacent rods (Fig. 1(e)). The interconnected adjacent nanorods are indicated by red ellipses in Fig. 1(e). It appears that the energy transferred from an incident ion to a nanorod induces intense local heating leading to melting and bending of the TiO$_2$ nanorods. Diffusion of the molten material between adjacent nanorods results in the formation of such interconnecting layers. Here, the individual nanorods having lateral dimensions of ~100 nm provide limited space for heat dissipation and molten state flow. Therefore, as a result of thermal spike induced melting, significant morphological changes are clearly observed from the FESEM images. However, in the case of polycrystalline films even if a thermal spike induced change in crystallinity occurs, it would not be so clearly evident through morphological changes. The digital photographs of actual samples irradiated at different fluences are shown in the ESI (Fig. S1†).

To investigate the structural changes induced by SHI irradiation, XRD analysis was carried out for pristine and irradiated samples, and the results are presented in Fig. 2(a). The XRD pattern of the pristine sample shows peaks at $36.10°$, $41.33°$, $54.59°$, $62.93°$ and $68.99°$, which correspond to (101), (111), (211), (002) and (301) of rutile TiO$_2$ (ICSD reference code 01-073-1765) respectively. The additional peaks are attributed to SnO$_2$ (ICSD reference code 01-077-0452) from the FTO coating of the substrate. After irradiation, there is a gradual reduction in crystallinity as indicated by decreasing intensities for (101), (211), and (002) peaks. To analyze the shift in the position of the peaks, a high-resolution X-ray scan was carried out for the (101) and (211) planes and the data are presented in Fig. 2(b) and (c), respectively. A clear shift to a lower 2θ value is observed, indicating an increase in the inter-planner spacing as a result of ion irradiation.

When high-energy ions pass through a material, an enormous amount of energy is transferred within a short period. As a result, in some cases, the amorphous material turns crystalline,[10] whereas the crystalline material becomes amorphous[13] due to thermal spike-induced heating, local melting, and ultrafast re-solidification. The excessive local heating along the ion trajectories creates latent ion tracks that are often distinct in density or crystallinity compared to the surrounding material. In the present case, the gradual decrease in crystallinity can be attributed to the increase in disorder resulting from the SHI-induced ion tracks that start overlapping with increasing ion fluence. Further, the shift of (101) and (211) peaks to lower diffraction angles after irradiation at a fluence of 1×10^{12} ions per cm^2 can be attributed to the ion irradiation-induced stresses in the TiO$_2$ lattice. The passage of energetic Ag ions causes atomic movements and vacancy creation in the lattice resulting in tensile stress leading to an expansion in the inter-planner spacing (d). Such an expansion causes a consequent shift of the XRD peak to a lower 2θ value.
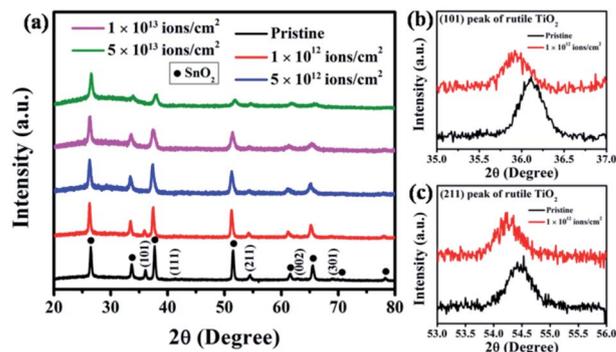
The changes in crystallinity were also studied by Raman spectroscopy, which is highly sensitive to the different crystalline phases of TiO$_2$. Fig. 3 presents the Raman spectra of the pristine and irradiated TiO$_2$ nanorods with different fluences.
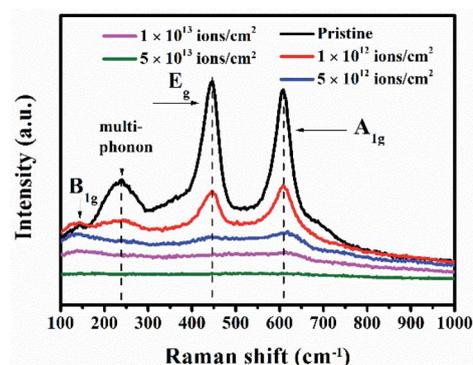
Fig. 3 Raman spectra of pristine and irradiated samples with 1×10^{12}, 5×10^{12}, 1×10^{13} and 5×10^{13} ions per cm^2 fluences. Dotted lines show the peak positions of the pristine sample and thus indicate slight shifts in the peak positions after irradiation.

The spectra for the pristine sample show three first-order Raman peaks at 143.91 cm^{-1} (B_{1g}), 444.85 cm^{-1} (E_g), and 608.62 cm^{-1} (A_{1g}) and a broad peak attributed to second-order scattering at 237.16 cm^{-1}, which correspond to the rutile TiO$_2$.[43,44] In all the Raman active modes, the Ti atom in the O–Ti–O bond remains at rest and vibration takes place at the oxygen atoms. The E_g mode is caused by the asymmetric bending of the O–Ti–O bonds in the {001} plane, where O atoms move in the opposite direction across the O–Ti–O bond and vibrate along the c-axis.[45] In contrast, the B_{1g} mode occurs as a result of the asymmetric bending of the O–Ti–O bonds in the {001}, {110} and {-110} planes. On the other hand, the A_{1g} mode arises due to the symmetric stretching of the O–Ti–O bonds in the {110} plane caused by the opposite directional movement of O atoms in the O–Ti–O bonds. In B_{1g} and A_{1g} modes, the O atoms move perpendicular to the c-axis with respect to the stationary Ti atom. The vibrations of oxygen atoms corresponding to each Raman mode are schematically[45] shown in Fig. S2 in the ESI.† It is observed that the peak intensities decrease gradually with the increase in ion fluences. This indicates a gradual loss of crystallinity in the TiO$_2$ lattice. In addition, there is a slight shift for B_{1g} at a fluence of 1×10^{12} ions per cm^2. As the ion fluence increases, the peak corresponding to A_{1g} mode shifts towards a higher frequency, while those of E_g and B_{1g} modes shift to lower frequencies. This results from the localized disorder and distortion of chemical bonds due to the oxygen vacancies in the TiO$_2$ octahedra,[46] which was also observed in a previous study.[30] In particular, compressive (or tensile) stress is known to cause a blue (or redshift) in the Raman peaks.[47] In our case, the blue shift of the A_{1g} peak indicates compressive stress perpendicular to the c-axis, which is caused by the shortening of Ti–O bonds. Gautam et al.[29] reported that the high density of oxygen vacancies in {110} planes results in tensile strain, which elongates the equatorial Ti–O bond and shortens the apical Ti–O bond. The shortening of apical Ti–O bond makes the bond stronger that leads to the blue shift of the A_{1g} peak.[29] On the other hand, the redshifts of B_{1g} and E_g modes suggest the development of tensile stress. The generation of compressive or tensile stresses is attributed to the non-uniform oxygen deficiency in the TiO$_2$ lattice caused by the energetic ion beam.[47] Further, it is observed that the relative intensity of E_g reduces compared to that of A_{1g}. The vertically aligned TiO$_2$ nanorods grow along the [001] direction.[48] Therefore, ion irradiation on the nanorods leads to a higher impact on the {001} planes compared to the others. Hence, the intensity of the E_g mode decreases rapidly as compared to that of the A_{1g} mode. Finally, at a fluence of 5×10^{13} ions per cm^2, the peaks almost disappear. This is correlated with the large density of defects and structural disorder created by the ion beam.

To further investigate the changes in the microstructure and crystallinity of the irradiated nanorods, we performed TEM analysis. The micrographs along with the selected area electron diffraction (SAED) patterns shown in insets are presented in Fig. 4. The TEM image of a single pristine nanorod showing an almost perfect tetragonal shape is presented in Fig. 4(a). The single-crystalline nature of this nanorod is confirmed from
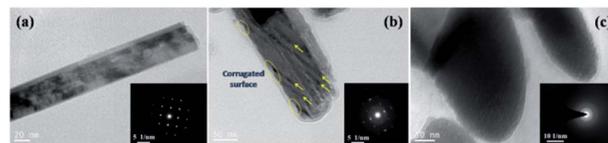
Fig. 4 TEM images and corresponding SAED patterns of (a) pristine and irradiated samples with (b) 5×10^{12} and (c) 5×10^{13} ions per cm^2 fluences. The arrows and yellow ellipses in (b) respectively indicate the ion tracks and the corrugated surface as a result of 100 MeV Ag ion irradiation (at a fluence of 5×10^{12} ions per cm^2).

a clear spot-type SAED pattern. The microstructure of the nanorods irradiated at a fluence of 5×10^{12} ions per cm^2 is presented in Fig. 4(b). In the SAED pattern, we observe diffused spots indicating an interruption in the long-range periodicity of the lattice. A closer look at the microstructure reveals striking features of parallel trajectories (indicated by yellow arrows) attributed to the track formation by SHI. The observed width of the tracks is ~10 nm, which is corroborated by the radial dimension of the simulated ion track obtained from the thermal spike model presented in the next section. Further, the smooth surface of the nanorod becomes corrugated (indicated by the yellow ellipse) at the sites of ion beam impingement. When the samples are irradiated at a fluence of 5×10^{13} ions per cm^2 (Fig. 4(c)), significant microstructural deformation takes place, as indicated by the ring-type SAED pattern. Here, we observe that the nanorods having rounded edges, which may be attributed to partial melting caused by a high amount of thermal energy resulting from the interaction with the ion beam.

Chemical compositions of pristine and irradiated nanorods were investigated by XPS. Fig. 5 presents (a) Ti 2p and (b) O 1s spectra of pristine and irradiated (5×10^{12} and 5×10^{13} ions per cm^2) samples. The peaks located at 457.47 eV and 463.06 eV (in Fig. 5(a)) are attributed to Ti 2p$_{3/2}$ and Ti 2p$_{1/2}$, respectively, and correspond to the Ti^{4+} state.[49] Fig. 5(a) shows no significant change in the peak position and shape after Ag ion irradiation.
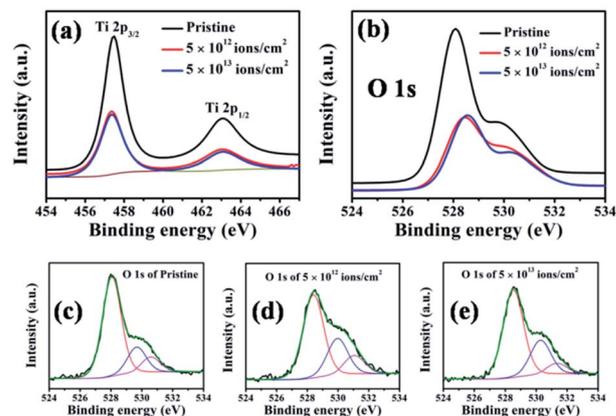
Fig. 5 XPS spectra (a) Ti 2p spectra and (b) O 1s spectra of pristine and irradiated samples at fluences of 5×10^{12} and 5×10^{13} ions per cm^2, (c), (d) and (e) present the fitted O 1s spectra of individuals.

However, the peak intensities decrease compared to that of pristine nanorods, which indicates a reduction in Ti^{4+} content in the sample.[50] The O 1s peak in Fig. 5(c) shows three components attributed to the lattice oxygen of TiO$_2$ (528.06 eV), oxygen vacancies (529.67 eV), and surface adsorbed oxygen (530.58 eV).[51] Fig. 5(b) shows that the contribution from oxygen vacancies becomes stronger in irradiated samples. After irradiation at fluences of 5×10^{12} ions per cm^2 and 5×10^{13} ions per cm^2, the peaks shift to the higher binding energies observed from Fig. 5(d) and (e). The peak positions in terms of binding energies (in eV) of Ti and O are presented in Table 1. The observed shift is attributed to the irradiation-induced changes in the electronic structure, as also observed in the case of ZnO nanorods.[52]

3.2. Thermal spike calculation

It is important to quantify the energy deposited by an irradiating ion to estimate the heat dissipation and thermal spike-induced effects in the material. To have a detailed analysis of the ion–matter interaction, the electronic and atomic (lattice) temperature evolution profiles were simulated in the framework of the inelastic thermal spike (i-TS) model.[53] The i-TS model considers the target material comprising two components, namely, electronic and atomic subsystems. The transient heat diffusion process between the incident ion and the two subsystems is well described by a set of coupled differential equations in a cylindrical geometry (r, z, t), which are as follows:[53]

$$C_e \frac{\partial T_e}{\partial t} = \nabla(K_e \times \nabla T_e) - g(T_e - \mathsf{T}_a) + A_e(r, t) \qquad (1)$$

$$C_a \frac{\partial T_a}{\partial t} = \nabla(K_a \times \nabla T_a) + g(T_e - T_a) + A_a(r, t) \qquad (2)$$

Here, r, z and t are the radial distance, depth and time, respectively. C_e and K_e are the specific heat and thermal conductivity of the electronic subsystem, whereas C_a and K_a represent the specific heat and thermal conductivity of the lattice, respectively. Electronic and lattice temperatures are denoted by T_e and T_a respectively. The energy deposited to the electrons in the target material through S_e (inelastic process) at a radial distance of r and at an instant of time t is taken into account by the term $A_e(r,t)$. In this study, S_n/S_e ($\sim$0.004) being $<10^{-2}$, the energy (S_n) deposited by the incident ion in the lattice ($A_a(r,t)$) is neglected.[53] The values of other relevant parameters used for the i-TS calculation are provided in the ESI (Table T2†). Here, it should be noted that when the dimensions reduce to

the nanoscale, both specific surface area and electronic properties (due to confinement) are drastically affected. In the present case, each nanorod is $\sim$100 nm wide and $\sim$1 μm in length. Therefore, the specific surface area certainly increases with respect to a polycrystalline thin film. However, in order to have significant changes in the electronic properties, strong quantum confinement is required, which, in the case of TiO$_2$ occurs at less than 1.5 nm dimensions.[54] Therefore, in spite of having nanostructure morphology, the bulk parameters are used for i-TS calculations since the dimensions are higher than that of the confinement regime.

Fig. 6(a) shows that the electronic subsystem retains the energy deposited by the incident ion for a very short period ($\sim 10^{-15}$ s) and then it is transferred to the lattice subsystem via electron–phonon coupling controlled by the parameter g. It is observed from Fig. 6(b) that the lattice temperature reaches the melting point of TiO$_2$ (2130 K)[27] at 5.5×10^{-15} s and the boiling point (3200 K)[27] at 2.3×10^{-14} s. Fig. 6(b) also shows that the temperature within a radius of 5.5 nm exceeds the melting point of 2130 K. This observation is in agreement with the lateral dimension ($\sim$10 nm) of the track as observed from high-resolution TEM images (Fig. 4(b)). According to the thermal spike model, the ion track appears as a consequence of the re-solidification during the rapid quenching of the molten state along the ion trajectory. Fig. 6(b) shows that the quenching from the molten state starts at 5.2×10^{-11} s, enabling us to ascribe the SHI-induced track formation to the rapid quenching of the thermal spike. Further, melting of the material as predicted by the i-TS model explains the observations in the SEM images (Fig. 1), which show a thin layer of material connecting the adjacent nanorods.

The interaction of the 100 MeV Ag ion beam with TiO$_2$ nanorod arrays is schematically shown in Fig. 7. At a relatively
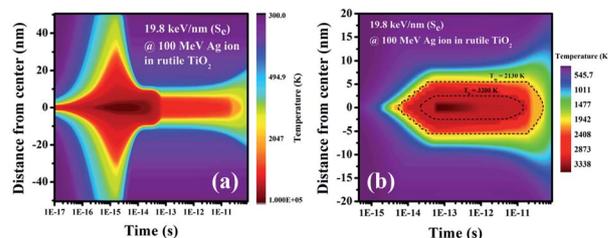
Fig. 6 (a) Electronic and (b) lattice temperature profiles along the radial distance from the center of the ion trajectory with the evolution of time.

Table 1 XPS peak positions in terms of binding energy (eV)

Chemical state of elements	Pristine	5 × 10^{12} ions per cm^2	5 × 10^{13} ions per cm^2
Ti 2p$_{3/2}$	457.47	457.34	457.34
Ti 2p$_{1/2}$	463.06	463.06	463.06
O 1s (lattice oxygen)	528.06	528.40	528.54
O 1s (oxygen vacancy)	529.67	529.96	530.27
O 1s (adsorbed oxygen)	530.58	531.05	531.33

lower fluence (5×10^{12} ions per cm²), tracks are formed inside the material preserving the tetragonal shape of each nanorod. However, at the highest fluence (5×10^{13} ions per cm²), individual ion tracks overlap that result in the overall melting of the nanorods. Being in a molten state, the nanorods start to bend and interconnect with adjacent nanorods through the diffusion of molten layers. Due to the rapid quenching of the molten state, significant distortions of the crystalline structure and the tetragonal shape occur along with the appearance of interconnected nanostructure morphology. Initially, TRIM simulation[42] (Fig. S3(c)†) was performed to quantify the disorder created inside the TiO₂ lattice. However, the TRIM code[42] does not account for the thermal spike phenomenon and therefore provides an under-estimation of the disorder compared to the experimental observations. In the present study, the disorderliness is highly pronounced as a consequence of thermal spike and rapid quenching.

3.3. Optical property study

The optical absorption of the pristine and irradiated TiO₂ nanorod arrays was characterized by diffuse reflectance spectroscopy. Fig. 8(a) and (b) show the diffuse reflectance and absorbance spectra of the pristine and irradiated samples with fluences of 5×10^{12} and 5×10^{13} ions per cm². To estimate the effective bandgap, the Kubelka–Munk function[55] was used to obtain the Tauc plot, as shown in Fig. 8(c). It is observed that the reflectance from the irradiated samples in the visible region is systematically reduced compared to that of pristine TiO₂ nanorod arrays. This suggests an enhancement in the visible light absorption that can be attributed to enhanced disorder caused by irradiation, which in turn leads to a higher surface area. Fig. 8(c) shows bandgap values obtained by the slope method, which are 3.11 eV for pristine and 3.23 eV for the sample irradiated at a fluence of 5×10^{12} ions per cm². On the other hand, the sample irradiated at 5×10^{13} ions per cm² shows an indirect bandgap of 3.10 eV (Fig. 8(d)). The position of the band edge at 3.11 eV for the pristine sample matches with the bandgap of rutile TiO₂.[8] It is reported that irradiation-
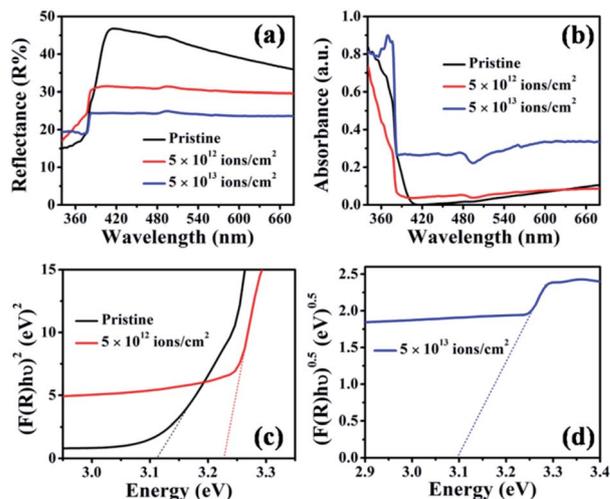
Fig. 8 (a) UV-Vis diffuse reflectance spectra, (b) absorbance spectra and (c and d) Tauc plots of pristine and samples irradiated at 5×10^{12} and 5×10^{13} ions per cm² fluences.

induced lattice distortion is mainly caused by oxygen vacancies.[30] The presence of the oxygen vacancies induces microstrain, as also observed from the XRD peak shift (Fig. 2). For the irradiation at a fluence of 5×10^{12} ions per cm², ion tracks lead to a structural distortion in the TiO₂ matrix. The reported optical bandgap value of the amorphous TiO₂ is 3.38 eV,[30] which is higher than that of rutile TiO₂. Therefore, the higher band edge position (compared to that of pristine) at 3.23 eV indicates a significant structural distortion in the irradiated samples. However, for the highest fluence (5×10^{13} ions per cm²), an indirect bandgap appears. The direct to indirect transition in the bandgap is also observed from the DFT-based analysis discussed in the subsequent section.

The luminescence characteristics of the pristine and irradiated nanorods were investigated by PL spectroscopy, and the
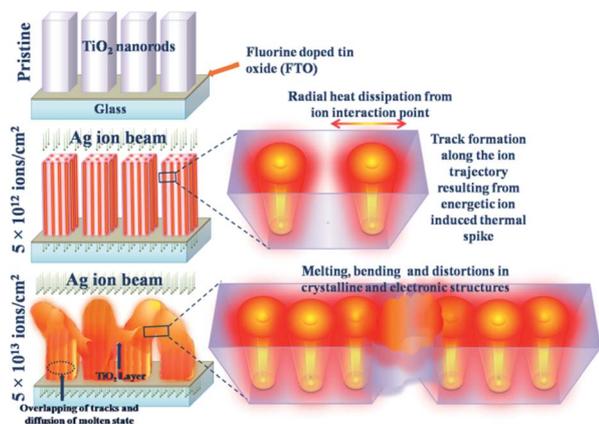
Fig. 7 Schematic presentation of the effect of high energy ion irradiation on the TiO₂ nanorods at different fluences (5×10^{12} ions per cm² and 5×10^{13} ions per cm²).
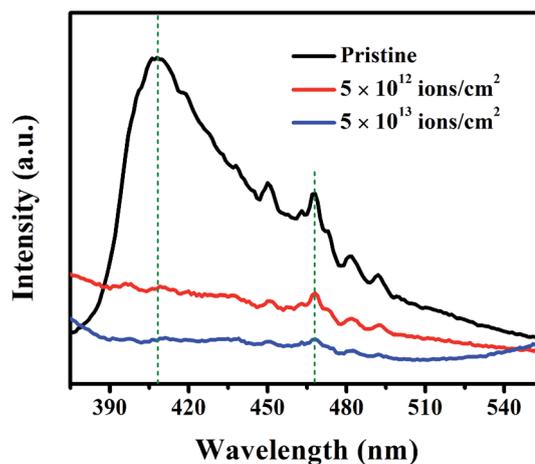
Fig. 9 PL spectra of pristine and irradiated samples with 1×10^{12}, 5×10^{12}, 1×10^{13} and 5×10^{13} ions per cm² fluences. 320 nm wavelength was used for excitation.

spectra are presented in Fig. 9. The PL spectrum of the pristine sample exhibits a prominent peak at 408 nm attributed to the near-band-gap emission and a peak at 467 nm, a characteristic peak for the rutile TiO_2.[56] Other small peaks at 450 nm, 482 nm, and 492 nm may arise from low-intensity radiative transitions between sub-band-gap states. The PL peaks do not show any significant shift after ion irradiation, but a decrease in intensities is observed. The peak at 408 nm is significantly reduced in intensity for the irradiated samples due to the incorporation of lattice defects and disorder build-up with increasing ion fluence. However, the peak at 467 nm suggests that some extent of the rutile structure persists even after the irradiation at the highest fluence of 5×10^{13} ions per cm^2.

3.4. Electronic structure using the DFT study

Insight into the transition from the direct to the indirect bandgap with irradiation-induced deformed structures can be obtained from the DFT calculations. The DFT methods for the periodic systems can be implemented because, despite deformation, periodicity remains in a larger domain as revealed by distinct XRD peaks. DFT studies on such systems can explain the effect of local distortion on the electronic structure.

The calculations have been performed using the plane-wave-pseudopotential approach as implemented in Quantum ESPRESSO.[57] The experimentally obtained lattice parameters of the tetragonal structure of the rutile TiO_2 estimated by Rietveld refinement of XRD data have been considered for the calculations. The Vanderbilt ultrasoft pseudopotentials are used to describe the electron–ion interactions,[58] in which the valence states of Ti include 12 electrons from 3s, 3p, 4s and 3d, and that of O includes 6 electrons from 2s and 2p shells. The exchange-correlation functional is approximated through the PBE-GGA functional.[59] The convergence criterion for self-consistent energy is taken to be 10^{-8} Ry. A k-mesh of $8 \times 8 \times 8$ is used for the Brillouin zone integration. The kinetic energy cut-off for the electron wave functions is set at 30 Ry, and the augmented charge density cut-off is set to be 300 Ry. Our previous analysis on TiO_2 tells that with these sets of parameters, the lattice parameters for the case of anatase TiO_2 match with that of the theoretical and experimental reports.[60,61]

The rutile TiO_2 crystallizes in a tetragonal structure with $P4_2/mnm$ (space group #136). Each unit cell contains two formula units of TiO_2, in which each Ti atom is coordinated with six O atoms and each O atom to three Ti atoms, as shown in Fig. 10(a). The TiO_2 octahedra are slightly distorted and connected at the edge through O atoms. In the present work, we have used the experimental lattice parameters obtained from the XRD data. For pristine TiO_2, the observed lattice parameters are $a = 4.575$ Å and $c = 2.936$ Å. When the structure is subjected to a fluence of 5×10^{12} ions per cm^2, the Ti–O bond undergoes slight distortion (Fig. 10(b)), indicating a structural transformation from the crystalline to the quasidisordered state. At a fluence of 5×10^{13} ions per cm^2, the structure undergoes a larger distortion which is clear from the breakdown of TiO_6 octahedra as presented in Fig. 10(c). Although the lattice parameter is hardly affected, the distortion of the Ti–O bond is
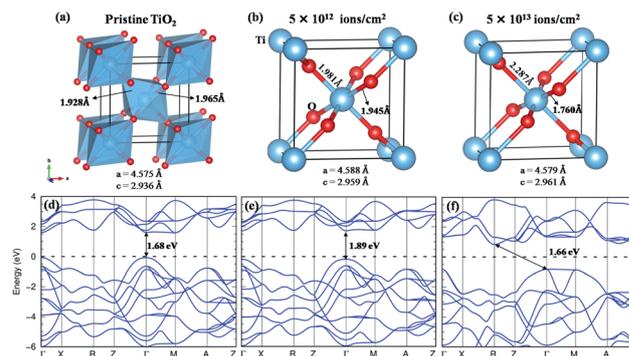
Fig. 10 (a) The structure of pristine rutile TiO_2 showing the corner-sharing TiO_6 octahedra. (b and c) The structure of TiO_2 when subjected to fluences of 5×10^{12} and 5×10^{13} ions per cm^2, respectively. It shows the change in the bond length of TiO_6 octahedra in the latter case. (d) The band structure of pristine rutile TiO_2 showing a direct bandgap of 1.68 eV with GGA calculation. (e and f) The band structure corresponding to (b) and (c) respectively. The Fermi level is set to be at zero. The Ti and O atoms are represented by light blue and red solid spheres, respectively.

quite significant, and its impact on the band structure is discussed in the following section.

With the GGA exchange-correlation functional, a direct bandgap is observed for pristine TiO_2 having a value of 1.68 eV with the band minima at the high symmetry point Γ (Fig. 10(d)). It is well understood that the GGA functional underestimates the bandgap.[62] Although the GGA + U can approximate the bandgap to the experimental value;[63] however, in the present situation, the GGA functional is sufficient to provide a comparison of the change in the bandgap with the structural deformation. At a fluence of 5×10^{12} ions per cm^2, a minor structural distortion takes place as a result of which the band dispersive nature remains almost like that of the pristine structure except for an increase in the bandgap by 0.21 eV (Fig. 10(e)). When the structure is subjected to a fluence of 5×10^{13} ions per cm^2, the band dispersion changes due to distortion of the Ti–O bond (Fig. 10(f)). It goes from the direct bandgap to the indirect bandgap system, where the valence band maxima are observed at Γ and M points and the conduction band minimum is at the R point. The intertwined Ti-d – O-p – Ti-d covalent interactions play a major role in the band dispersion of the lower-lying conduction bands. The increase in bond length and further tilting of the Ti–O–Ti axis modify this interaction to create the CBM at R instead of Γ. Such a direct to indirect transition of the bandgap has also been observed in ZnO and Si nanowires.[64–66]

4. Conclusions

We have reported the effect of 100 MeV Ag ion beam irradiation on vertically oriented TiO_2 nanorods grown on an FTO coated glass substrate. The nanorods undergo a significant morphological and structural transformation through bending and melting induced by a localized thermal spike, particularly at the highest fluence (5×10^{13} ions per cm^2). High-resolution TEM analysis shows tracks with a lateral dimension of ∼10 nm along

the ion trajectory. Thermal spike simulation confirms the melting in TiO_2 nanorods within a cylindrical region having a radius of ~ 5.5 nm, supporting the TEM observation. Resolidification during the rapid quenching of the SHI-induced thermal spike within a time interval of ~ 0.5 picoseconds is responsible for the deformation of the crystalline structure, as also observed in the XRD and Raman data. XPS analysis reveals the presence of ion beam-induced vacancies in the lattice, and the resulting strain is manifested by the shift in XRD and Raman peaks. An interesting feature of the irradiation is the transition from a direct to an indirect bandgap at the highest fluence (5×10^{13} ions per cm^2), which is also supported by the electronic band structure calculation using DFT. Hence, the localized modification of the TiO_2 nanorods induced by high energy ion beam irradiation offers unique features in terms of crystallinity, morphology and electronic band structure.

Conflicts of interest

There are no conflicts to declare.

Acknowledgements

References

1 M. K. Nowotny, L. R. Sheppard, T. Bak and J. Nowotny, *J. Phys. Chem. C*, 2008, **112**, 5275–5300.

2 S. Wang, L. Pan, J. J. Song, W. Mi, J. J. Zou, L. Wang and X. Zhang, *J. Am. Chem. Soc.*, 2015, **137**, 2975–2983.

3 D. Kanjilal, *Curr. Sci.*, 2001, **80**, 1560–1566.

4 C. Notthoff, S. Jordan, A. Hadley, P. Mota-Santiago, R. G. Elliman, W. Lei, N. Kirby and P. Kluth, *Phys. Rev. Mater.*, 2020, **4**, 046001.

5 N. A. Nebogatikova, I. V. Antonova, S. V. Erohin, D. G. Kvashnin, A. Olejniczak, V. A. Volodin, A. V. Skuratov, A. V. Krasheninnikov, P. B. Sorokin and L. A. Chernozatonskii, *Nanoscale*, 2018, **10**, 14499–14509.

6 L. Madauß, I. Zegkinoglou, H. Vázquez Muiños, Y. W. Choi, S. Kunze, M. Q. Zhao, C. H. Naylor, P. Ernst, E. Pollmann, O. Ochedowski, H. Lebius, A. Benyagoub, B. Ban-D'Etat, A. T. C. Johnson, F. Djurabekova, B. Roldan Cuenya and M. Schleberger, *Nanoscale*, 2018, **10**, 22908–22916.

7 M. Toulemonde, C. Trautmann, E. Balanzat, K. Hjort and A. Weidinger, *Nucl. Instrum. Methods Phys. Res., Sect. B*, 2004, **216**, 1–8.

8 P. Roy, S. Berger and P. Schmuki, *Angew. Chem., Int. Ed.*, 2011, **50**, 2904–2939.

9 N. Khatun, S. Tiwari, C. P. Vinod, C. M. Tseng, S. Wei Liu, S. Biring and S. Sen, *J. Appl. Phys.*, 2018, **123**, 245702.

10 M. Thakurdesai, D. Kanjilal and V. Bhattacharyya, *Appl. Surf. Sci.*, 2008, **254**, 4695–4700.

11 M. Thakurdesai, T. Mohanty, D. Kanjilal, P. Raychaudhuri and V. Bhattacharyya, *Appl. Surf. Sci.*, 2009, **255**, 8935–8940.

12 M. Thakurdesai, D. Kanjilal and V. Bhattacharyya, *Semicond. Sci. Technol.*, 2009, **24**, 085023.

13 R. Hazem, M. Izerrouken, A. Sari, S. Kermadi, M. Msimanga, A. Benyagoub, M. Maaza, M. Belgaid and M. Boumaour, *Nucl. Instrum. Methods Phys. Res., Sect. B*, 2013, **304**, 16–22.

14 H. Rath, P. Dash, T. Som, P. V. Satyam, U. P. Singh, P. K. Kulriya, D. Kanjilal, D. K. Avasthi and N. C. Mishra, *J. Appl. Phys.*, 2009, **105**, 074311.

15 S. Gautam, K. H. Chae, H. Thakur, R. Kumar, P. Thakur, N. B. Brookes and K. K. Sharma, *J. Appl. Phys.*, 2011, **110**, 083718.

16 S. K. Gautam, A. Chettah, R. G. Singh, S. Ojha and F. Singh, *Nucl. Instrum. Methods Phys. Res., Sect. B*, 2016, **379**, 224–229.

17 M. Thakurdesai, A. Mahadkar, D. Kanjilal and V. Bhattacharyya, *Vacuum*, 2008, **82**, 639–644.

18 R. Sanz, J. Jensen, A. Johansson, M. Skupinski, G. Possnert, M. Boman, M. Hernandez-Vélez, M. Vazquez and K. Hjort, *Nanotechnology*, 2007, **18**, 305303.

19 K. ichi Nomura, T. Nakanishi, Y. Nagasawa, Y. Ohki, K. Awazu, M. Fujimaki, N. Kobayashi, S. Ishii and K. Shima, *Phys. Rev. B: Condens. Matter Mater. Phys.*, 2003, **68**, 064106.

20 J. Jensen, M. Skupiński, K. Hjort and R. Sanz, *Nucl. Instrum. Methods Phys. Res., Sect. B*, 2008, **266**, 3113–3119.

21 K. Awazu, M. Fujimaki, Y. Ohki and T. Komatsubara, *Radiat. Meas.*, 2005, **40**, 722–729.

22 M. Karlušić, M. Jakšić, H. Lebius, B. Ban-D'Etat, R. A. Wilhelm, R. Heller and M. Schleberger, *J. Phys. D: Appl. Phys.*, 2017, **50**, 205302.

23 M. Karlušić, S. Bernstorff, Z. Siketic, B. Šantic, I. Bogdanovic-Radovic, M. Jakšic, M. Schleberger and M. Buljan, *J. Appl. Crystallogr.*, 2016, **49**, 1704–1712.

24 J. H. O'Connell, V. A. Skuratov, A. Akilbekov, A. Zhumazhanova and A. Janse Van Vuuren, *Nucl. Instrum. Methods Phys. Res., Sect. B*, 2016, **379**, 200–205.

25 J. O'Connell, V. Skuratov, A. J. van Vuuren, M. Saifulin and A. Akilbekov, *Phys. Status Solidi B*, 2016, **253**, 2144–2149.

26 J. H. O'Connell, G. Aralbayeva, V. A. Skuratov, M. Saifulin, A. Janse Van Vuuren, A. Akilbekov and M. Zdorovets, *Mater. Res. Express*, 2018, **5**, 055015.

27 K. Awazu, X. Wang, M. Fujimaki, T. Komatsubara, T. Ikeda and Y. Ohki, *J. Appl. Phys.*, 2006, **100**, 044308.

28 P. Zhai, S. Nan, L. Xu, W. Li, Z. Li, P. Hu, J. Zeng, S. Zhang, Y. Sun and J. Liu, *Nucl. Instrum. Methods Phys. Res., Sect. B*, 2019, **457**, 72–79.

29 S. K. Gautam, F. Singh, I. Sulania, R. G. Singh, P. K. Kulriya and E. Pippel, *J. Appl. Phys.*, 2014, **115**, 143504.

30 H. Rath, P. Dash, U. P. Singh, D. K. Avasthi, D. Kanjilal and N. C. Mishra, *Nucl. Instrum. Methods Phys. Res., Sect. B*, 2015, **365**, 553–559.

31 J. Deng, Y. Su, D. Liu, P. Yang, B. Liu and C. Liu, *Chem. Rev.*, 2019, **119**, 9221–9259.

32 M. Wang, J. Duan, J. Du, X. Yang, Y. Duan, T. Zhang and Q. Tang, *ACS Appl. Mater. Interfaces*, 2021, **13**, 12091–12098.

33 J. W. Yoon, D. H. Kim, J. H. Kim, H. W. Jang and J. H. Lee, *Appl. Catal., B*, 2019, **244**, 511–518.

34 J. I. Jang, Y. H. Shin, Y. S. Kim, A. D. Nguyen, T. H. Pham, T. K. Nguyen, H. Ullah, Z. Tahir, Y. C. Park and J. Park, *ACS Appl. Energy Mater.*, 2020, **3**, 10854–10862.

35 D. Wang, L. Chen, Z. Ding and X. Feng, *Sol. RRL*, 2019, **4**, 1900185.

36 Y. Gao, J. Xu, S. Shi, H. Dong, Y. Cheng, C. Wei, X. Zhang, S. Yin and L. Li, *ACS Appl. Mater. Interfaces*, 2018, **10**, 11269–11279.

37 H. K. Ramamurthy Rao, E. Gemechu, U. Thakur, K. Shankar and A. Kumar, *Sol. Energy Mater. Sol. Cells*, 2021, **230**, 111288.

38 X. Feng, K. Shankar, O. K. Varghese, M. Paulose, T. J. Latempa and C. A. Grimes, *Nano Lett.*, 2008, **8**, 3781–3786.

39 M. Zu, M. Zheng, S. Zhang, C. Xing, M. Zhou, H. Liu, X. Zhou and S. Zhang, *Sens. Actuators, B*, 2020, **321**, 128504.

40 S. Dey and S. C. Roy, *Nano Express*, 2021, **2**, 010028.

41 D. Kanjilal, S. Chopra, M. M. Narayanan, I. S. Iyer, V. Jha, R. Joshi and S. K. Datta, *Nucl. Instrum. Methods Phys. Res., Sect. A*, 1993, **328**, 97–100.

42 J. F. Ziegler, M. D. Ziegler and J. P. Biersack, *Nucl. Instrum. Methods Phys. Res., Sect. B*, 2010, **268**, 1818–1823.

43 S. Dey and S. C. Roy, *J. Alloys Compd.*, 2021, **881**, 160481.

44 M. Li, X. Zhang, Y. Liu and Y. Yang, *Appl. Surf. Sci.*, 2018, **440**, 1172–1180.

45 Y. Zhang, C. X. Harris, P. Wallenmeyer, J. Murowchick and X. Chen, *J. Phys. Chem. C*, 2013, **117**, 24015–24022.

46 H. Rath, B. N. Dash, A. Benyagoub and N. C. Mishra, *Sci. Rep.*, 2018, **8**, 11774.

47 R. Hazem, M. Izerrouken, A. Cheraitia and A. Djehlane, *Nucl. Instrum. Methods Phys. Res., Sect. B*, 2019, **444**, 62–67.

48 H.-H. Chou, S. Y.-H. Liou and M. Calatayud, *Catal. Today*, 2020, **356**, 49–55.

49 B. Bharti, S. Kumar, H. N. Lee and R. Kumar, *Sci. Rep.*, 2016, **6**, 32355.

50 A. Manna, A. Barman, S. R. Joshi, B. Satpati, P. Dash, A. Chattaraj, S. K. Srivastava, P. K. Sahoo, A. Kanjilal, D. Kanjilal and S. Varma, *J. Appl. Phys.*, 2018, **124**, 155303.

51 J. Li, H. Zhou, H. Zhuo, Z. Wei, G. Zhuang, X. Zhong, S. Deng, X. Li and J. Wang, *J. Mater. Chem. A*, 2018, **6**, 2264–2272.

52 K. S. Ranjith, L. R. Nivedita, K. Asokan, S. Krishnamurthy, R. Pandian, M. Kamruddin, D. K. Avasthi and R. T. Rajendra Kumar, *Sci. Rep.*, 2017, **7**, 3251.

53 C. Dufour, V. Khomenkov, G. Rizza and M. Toulemonde, *J. Phys. D: Appl. Phys.*, 2012, **45**, 065302.

54 S. Monticone, R. Tufeu, A. V. Kanaev, E. Scolan and C. Sanchez, *Appl. Surf. Sci.*, 2000, **162**, 565–570.

55 S. Dey and S. C. Roy, *Ceram. Int.*, 2021, **47**, 14603–14611.

56 M. Maria Angelin Sinthiya, N. Kumaresan, K. Ramamurthi, K. Sethuraman, S. Moorthy Babu, R. Ramesh Babu and V. Ganesh, *Appl. Surf. Sci.*, 2018, **449**, 122–131.

57 P. Giannozzi, *J. Phys. Condens. Matter*, 2017, **29**, 465901.

58 D. Vanderbilt, *Phys. Rev. B: Condens. Matter Mater. Phys.*, 1990, **41**, 7892–7895.

59 J. P. Perdew, K. Burke and M. Ernzerhof, *Phys. Rev. Lett.*, 1996, **77**, 3865–3868.

60 S. B. Mishra, A. Choudhary, S. C. Roy and B. R. K. Nanda, *Phys. Rev. Mater.*, 2018, **2**, 115801.

61 S. B. Mishra and B. R. K. Nanda, *Appl. Surf. Sci.*, 2020, **531**, 147330.

62 S. Di Mo and W. Y. Ching, *Phys. Rev. B: Condens. Matter Mater. Phys.*, 1995, **51**, 13023–13032.

63 S. B. Mishra, S. C. Roy and B. R. K. Nanda, *Appl. Surf. Sci.*, 2021, **542**, 148709.

64 S. Li, J. L. Li, Q. Jiang and G. W. Yang, *J. Appl. Phys.*, 2010, **108**, 024302.

65 L. Shi and G. Zhang, *J. Electron. Mater.*, 2016, **45**, 5391–5394.

66 I. J. T. Jensen, A. G. Ulyashin and O. M. Løvvik, *J. Appl. Phys.*, 2016, **119**, 015702.